High-efficiency Fe-Mediated Bi_2MoO_6 nitrogen-fixing photocatalyst: Reduced surface work function and ameliorated surface reaction

Qingqiang Meng[a], Chade Lv[a], Jingxue Sun[a],[*], Weizhao Hong[a], Weinan Xing[b], Liangsheng Qiang[a], Gang Chen[a],[*], Xiaoli Jin[a]

[a] MIIT Key Laboratory of Critical Materials Technology for New Energy Conversion and Storage, School of Chemistry and Chemical Engineering, Harbin Institute of Technology, Harbin, 150001, China
[b] College of Biology and the Environment, Nanjing Forestry University, Nanjing, 210037, China

ABSTRACT

Rapid carrier transport and efficient surface reactions are key factors for improving photocatalytic nitrogen fixation. Herein, an efficient Bi_2MoO_6 nitrogen-fixing photocatalyst was obtained using Fe-mediation. The Fe-doping induced surface work function reduction would boost the charge transport to the surface of catalyst. Besides that, the Fe-doping can also improve the charge collection through a Fe^{3+}/Fe^{2+} redox pathway, which serves as active sites for nitrogen reduction. Thanks to above merits, Fe-mediated Bi_2MoO_6 exhibits dramatically enhanced visible-light-driven photocatalytic activity for nitrogen fixation, in sharp contrast with pristine Bi_2MoO_6. This work provides a new approach to improve photocatalytic nitrogen reduction reaction, which can pave the way for modification studies in nitrogen fixation photocatalysts.

1. Introduction

Nitrogen fixation is a vital important chemical process in nature since nitrogen is an indispensable element for most biomolecules to sustain life. [1,2] In recent years, many nitrogen-fixing technologies have been developed, such as electrocatalytic nitrogen fixation, photocatalytic nitrogen fixation, and photocatalytic nitrogen fixation [3–6]. Among them, photocatalytic nitrogen fixation technology has become a hot research topic because of its advantages of energy conservation and environment-friendly features. Photocatalytic nitrogen fixation is considered to be a promising alternative to the traditional Haber-Bosch process. However, the development of efficient photocatalysts still remains a challenge for its further practical application [7–11]. In a typical photocatalytic reaction, the dynamic behavior of photogenerated carriers, that is, the velocity of carrier migration and surface reactions plays an important role in performance of photocatalysts [12–16]. Therefore, to optimize the dynamic behavior of photogenerated carriers, many efforts have been dedicated, such as constructing heterojunctions, regulating nanostructure, coupling noble metal, and doping heteroatom *etc* [17,18]. Particularly, the heteroatom doping strategy is a facile and effective method to improve the photocatalytic activity [19–23]. Most researches of dopant engineering are focusing on the extending optical response range, increasing surface

area of the raw nanomaterials [24–26]. However it should also be considered that the effect on the surface reaction and the electrodynamic behavior of materials after doping.

It has been observed that the nitrogen fixation reaction of photocatalysts can be promoted by doping modification, such as Ce, V, Co, Mo, Ni, *etc*. [27] Especially, Fe^{3+} is one of the most widely studied transition metal ions owing to its low cost and excellent effect. [28–30] Until now, several studies have indicated that the doping of photocatalyst with Fe^{3+} ions can significantly enhance its photocatalytic nitrogen fixation activity. Zhao et al. speculated that the Fe^{3+} acted as the intermediate to promote the transfer of electrons and holes. [31] Soria et al. proposed that Fe^{3+} ions could provisionally trap photogenerated electrons and promote the separation of charge carriers, resulting in enhanced N_2 fixation performance. [32] Therefore, it is necessary to further study the intrinsic causes of photocatalytic activity improvement caused by transition metal ion doping modification.

The surface work function is an important physical parameter that directly reflects the dynamic behavior of electrons. Generally, the surface work function is often referred to as metal work function, which can reflect the ability of the solid surface to donate free electrons. [33,34] Similarly, for a typical semiconductor, it can be described as the ability of photo-induced electrons transport to surface to proceed the photocatalytic reaction. It is widely accepted that the value of

surface work function is determined by the concentration of impurities in the crystal of semiconductor. Sun et al. research shows that the electrons in b-TiO_2/MoS_2/CdS composite semiconductors are more likely to migrate to the surface compared with pure phase samples by investigating their surface work function. [35] Ran et al. studied the migration direction of electrons between phosphorene and g-C_3N_4 by analyzing the surface work function of materials. [36] Hence, it is achievable to tune the surface work function of semiconductors by doping heteroatom into crystal lattice to improve the dynamic behavior of photogenerated carriers.

In this work, we construct a Fe-doped Bi_2MoO_6 photocatalyst through a facile solvethermal method. The Fe-doping to endow the catalyst with superior N_2 fixation ability ascribed to the Fe-doping can reduce the surface work function of Bi_2MoO_6 to facilitate the charge migration to the surface. In addition, the introduction of Fe^{3+}/Fe^{2+} redox pathway, which can serve as surface centers for N_2 reduction. Due to these factors, Fe-doped Bi_2MoO_6 realizes remarkably improved photocatalytic activity for nitrogen fixation, which is a 3.7 times higher relative to pristine Bi_2MoO_6. The presented work offers a new mechanism to enhance the charge collection for rapid photogenerated charge carriers separation and transport.

2. Experimental Section

2.1. Synthesis of Fe-doping Bi_2MoO_6

Typically, $Bi(NO_3)_3 \cdot 5H_2O$ (1 mmol) and $Na_2MoO_4 \cdot 2H_2O$ (0.5 mmol) were dissolved in 5 ml of ethylene glycol (EG) separately with vigorous stirring to form a clear solution. Subsequently, the two pellucid solutions were mixed together and the mixed solution was added dropwise to 20 ml C_2H_5OH. Then a certain amounts (0%, 0.3%, 0.5%, and 1% molar ratio of Fe to Bi atoms) of $Fe(NO_3)_3$ were dissolved in the above solution under stirring for 30 min. After that, the mixed solution was solvothermally treated at 160 °C for 24 h in a 50 ml Teflon-lined stainless steel autoclave. After cooling down to the room temperature, the obtained sample was washed with deionized water and ethanol three times and dried at 80 °C for 12 h. The samples were defined as BMO, 0.3% Fe-BMO, 0.5% Fe-BMO and 1.0% Fe-BMO, respectively.

2.2. Characterization

Powder X-ray diffraction (XRD) patterns were carried out on a Rigaku D/max-2000 equipped with Cu-Kα radiation (λ = 1.5418 Å). Field-emission scanning electron microscopy (FESEM, FEI QUANTA 200 F, accelerating voltage = 10 kV) and Transmission electron microscopy (TEM FEI Tecnai G2 S-Twin) were employed to characterize the structure and morphology of the samples. Raman spectroscopy was recorded by a Jobin Yvon HR 800 micro-Raman spectrometers at 457.9 nm. X-Ray photoelectron spectroscopy (XPS) was carried out on a Thermo Scientific ESCALAB 250Xi X-ray photoelectron spectrometer. The specific surface area of the samples was tested on a Micromeritics Tristar II and calculated by the Brunauer-Emmett-Teller (BET) method. The UV–vis diffuse reflectance spectra (DRS) datas were recorded on the HITACHI UH4150 using $BaSO_4$ as the reflectance standard sample. The photoluminescent and fluorescence lifetime were measured using the lifetime spectrofluorometer (HORIBA Fluoromax-4) with a pulsed light-emitting diode (LED, λ = 301 nm) as the excitation light source. The work function measurement was performed on a SKP 5050 K probe measurement system.

2.3. Photocatalytic nitrogen fixation

The photocatalytic nitrogen fixation was evaluated under visible light. The image of reaction device as shown in Fig. S1. Typically, 0.05 g catalyst was uniformly dispersed into the deionized water (100 ml Multiple distillation to remove NH_3) by ultrasound. A 300 W Xe lamp

was served as visible-light source with a filter (λ > 400 nm). The flow rate of nitrogen is maintained at 100 ml min^{-1}. Before irradiation, the suspension was stirred for 30 min in dark. During irradiation, 3 ml suspension was collected every 20 min, then centrifuged to remove the photocatalyst for measured by UV–vis spectrophotometer (HITACHI UH-5300) with Nessler's reagent. [37,38]

2.4. Photocatalytic reduction of Cr(VI)

The photocatalytic reduction of Cr(VI) was evaluated under visible light. Typically, the photocatalytic reduction of Cr(VI) was executed in a quartz reactor containing 0.05 g catalyst, 0.05 g citric acid (as the hole trapping agent) and 100 ml containing Cr(VI) solution (10 mg L^{-1}). A 300 W Xe lamp was served as visible-light source with a filter (λ > 400 nm). First, the suspension was stirred for 30 min in dark to establish an adsorption-desorption equilibrium. During irradiation, 5 ml suspension was collected every 5 min for photo-reduction Cr(VI), then centrifuged to remove the photocatalyst for measured by UV–vis spectrophotometer (HITACHI UH-5300). After each cycle, the catalyst was recollected by centrifugation and washing, then tested the next cycle.

2.5. Photoelectrochemical measurements

Photoelectrochemical measurements were implemented by an electrochemical working station (AUT-86258) in a standard three-electrode system with the Ag/AgCl as a reference electrode, the Pt sheet as a counter electrode and the samples coated at FTO glass as a working electrode, reference electrode and counter-electrode, respectively. A 300 W Xe lamp with a visible light filter (λ > 400 nm) served as light source and 0.1 M Na_2SO_4 solution was used as the electrolyte.

3. Results and discussion

BMO and Fe-BMO samples with different ratios of Fe:Bi were synthesized *via* a solvothermal method. As presented in Fig. S2a, the morphology of pristine BMO shows a hollow microsphere structure assembled by nanosheets and with a diameter of 1.5 μm. As increasing the Fe^{3+} addition, yolk-shell structure is formed as well as the gradually increasing size to around 3 μm (Fig. 1a and b; Fig. S2b and c and Fig. S3). The HRTEM image of a representative sample 0.5% Fe-BMO (Fig. 1c) displays sequential and vertical lattice fringes with the interplanar spacings of 0.270 nm and 0.273 nm corresponding to (002) and (060), respectively. [39] The corresponding fast Fourier transform selected area electron diffraction pattern reveals an orthorhombic Bi_2MoO_6 on the (100) projection (Fig. 1d), indicating the nanosheets are exposed with the (100) crystal face to assemble the microspheres. According to the EDX mapping analysis, the Bi, Mo, O and Fe are distributed uniformly in 0.5% Fe-BMO, which manifests the presence of Fe element in Bi_2MoO_6. (Fig. 1e and f).

To determine the Fe-doping, X-ray diffraction (XRD) analysis is employed. As observed in Fig. 2a, the XRD patterns of Fe-BMO samples present similar diffraction peak positions with pristine BMO (JCPDS Card No. 77-1426), [40–42] while no other phases can be distinguished, demonstrating that the introduction of Fe^{3+} results in doping rather than the formation of $BiFeO_3$. Moreover, the gradual shifts of (131) peak and (002) peak observed in the magnified XRD patterns can further affirm the Fe^{3+} doping (Fig. 2b and c). Aiming at detect the chemical state of Fe^{3+} doping in Fe-BMO sample, X-ray photoelectron spectroscopy (XPS) was conducted. As shown in Fe 2p spectra (Fig. 2g), two weak signals (711.3 and 724.3 eV,) can be observed in 0.5% Fe-BMO, while the pristine BMO presents no Fe^{3+} peaks in the observation region. The separation distance between above two peaks is 13.0 eV, which confirms the Fe^{3+} state of iron in Fe-doped Bi_2MoO_6 [43,44]. For Bi 4f XPS spectra (Fig. 2d), two characteristic peaks of BMO locate at the binding energies of 159.1 and 164.5 eV
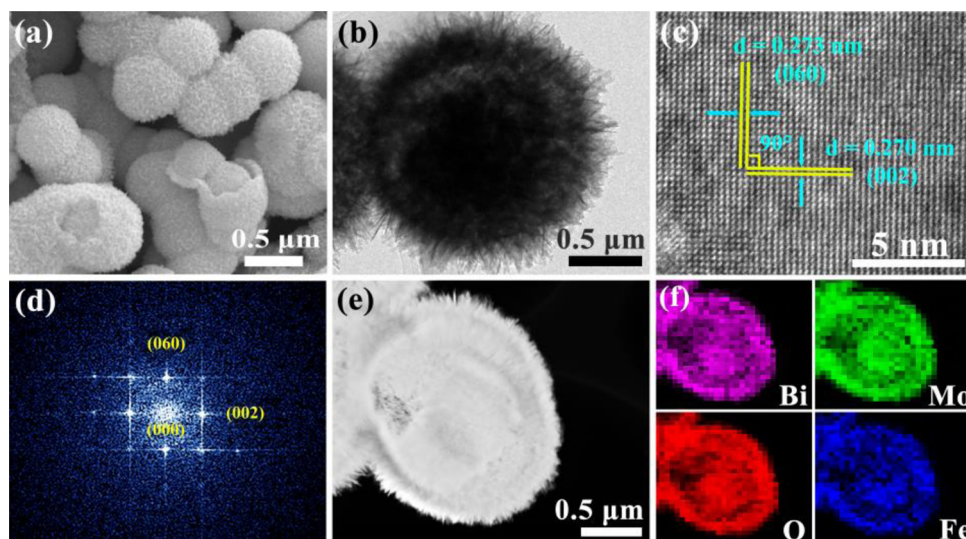
Fig. 1. (a) SEM image, (b) TEM, (c) HRTEM image, (d) Fourier transform electron diffraction patterns, (e) HADDF STEM image, and (f) STEM mapping of 0.5% Fe-BMO.

assignable to Bi $4f_{7/2}$ and Bi $4f_{5/2}$ of Bi^{3+} ions, respectively. [20,21,45–51] Conspicuously, the Bi 4f peaks of 0.5% Fe-BMO shift slightly to higher values relative to BMO. Moreover, similar shifts in the binding energies of Mo 3d and O 1s are also observed in the XPS spectra of Fe-doped BMO (Fig. 2e and f), [23,52–55] which is mainly attributed to a higher electronegativity of Fe^{3+} than that of Bi^{3+}. Therefore, Fe^{3+} is more attractive to electrons, leading to the electron migration to Fe^{3+} ion and the reduction of Bi binding energy. Furthermore, as the radius of Fe^{3+} is smaller than that of Bi^{3+}, the Fe^{3+} ions prefer to occupy the Bi^{3+} sites Bi_2MoO_6. Based on the calculation (details are presented in Supporting Information), the formation energy of Fe^{3+} doping at Bi^{3+} sites is reduced by 13.06 eV per slab compared to the unsubstituted sample (structural models are shown in Fig.S4). This speculation is further confirmed by the Raman characterization. As shown in Fig. S5, all the Fe-BMO samples exhibit the specific vibration mode of BMO, and the bond lengths of Mo-O in MoO_6 octahedron are not changed because their corresponding stretching frequency has not shifted. [56] Therefore, it can be concluded that Fe^{3+} replaces Bi^{3+} to form Fe-Mediated Bi_2MoO_6 photocatalyst.

In order to verify the effect of Fe^{3+} doping on catalytic activity, photocatalytic nitrogen fixation was performed under visible light irradiation. The nitrogen fixation rate of the samples are calculated according to the standard curve: y = 0.00176x + 0.02428 (Fig. S6). As shown in Fig. 3a, the 0.5% Fe-BMO exhibits the optimal photocatalytic activity among the samples. With the absence of sacrificial reagent, the average nitrogen fixation rate of the 0.5% Fe-BMO was 106.5 μmol $g^{-1} h^{-1}$, which is 3.7 times higher than that of BMO. At the same time, the stabilities of the 0.5% Fe-BMO as photocatalysts for nitrogen photofixation was evaluated in a cyclic test experiment with five-cycles. As depicted in Fig. 3b, it is clearly seen that the 0.5% Fe-BMO presented a very stable performance for nitrogen photofixation over repeated cycling. There was no significant change of the crystal phase and morphology (Fig. S7–8) after five cycles, suggesting that the sample has good chemical and photochemical stability. The photocatalytic nitrogen fixation performance was further verified by indophenol blue method and ion chromatography method. As shown in Fig.S9, the results of the three detection methods are highly consistent. At the same time, the 0.5% Fe-BMO exhibited excellent selectivity to generate NH_3 because the yield of N_2H_4 was much lower than that of NH_3 after 120 min of illumination (Fig. S10–11). Ulteriorly, to confirm the source of N element, we carried out a photocatalytic experiment under different reaction conditions as shown in Fig. S12. There was no ammonia detected under the conditions of Ar atmosphere, air atmosphere and without

photocatalyst. Meanwhile, the 0.5% Fe-BMO exhibited excellent photocatalytic nitrogen fixation activity when the catalyst was present and the N_2 atmosphere. This further indicates that the N element is derived from the incoming N_2. Furthermore, to analyze the contribution of specific surface area to the photocatalytic performance of the samples, we tested the specific surface area of the samples as shown in Fig. 3c. Simultaneously, the photocatalytic nitrogen fixation performance are normalized according to the specific surface areas of BMO and 0.5% Fe-BMO (Fig. 3d). The nitrogen fixation activity of 0.5% Fe-BMO is still much higher in contrast with that of BMO after normalization. Therefore, the increased specific surface area does not play the key role in improving the photocatalytic activity of 0.5% Fe-BMO. In addition, we also carried out photocatalytic reduction of

Cr(VI) to further verify the improvement of photocatalytic activity of BMO by Fe^{3+} doping. As shown in Fig. S13, the doped samples all exhibited better performance than the original samples and exhibited excellent photocatalytic stability. Based on the above analysis, it is further confirmed that the half-reaction of electrons is promoted by the introduction of hetero-atoms Fe in the BMO lattice.

To explore the key factors for the improvement in photocatalytic activity after Fe^{3+} doping, the light absorption ability is resolved by UV–vis diffuse reflectance spectroscopy (DRS). As shown in Fig. 4a, the absorption edge of BMO samples display red shift from 475 nm to 521 nm as increasing the amounts of Fe^{3+} doping. The calculated bandgap values of Fe-BMO samples reduce from 2.61 to 2.36 eV, which are converted from the plots of $(ahv)^2$ against (hv) (Fig. 4b). According to the XPS valence-band spectra, the valence band maximum (VBM) position of 0.5% Fe-BMO is consistent with that of BMO (Fig. 4c). The XPS valence band characterization of the samples show that the position of the valence band have not moved (Fig. 4d). Therefore, the detailed electronic band structures before and after Fe^{3+} doping were identified shown in Fig. 4e. Based on the above results, new energy levels (doping level) are formed on the bottom of the conduction band to narrow the bandgap of BMO. Further, we performed photocatalytic nitrogen fixation on BMO and 0.5% Fe-BMO samples under visible light irradiation (λ > 500 nm). As shown in Fig. 4f, 0.5% Fe-BMO exhibits a certain photocatalytic activity, whereas BMO can not carry out nitrogen fixation under the same condition. This indicates that the enhancement of optical absorption caused by Fe^{3+} doping has a certain contribution but not the main factor to the improvement in photocatalytic activity.

To analyze the surface electronic properties after Fe-doping, which is related to the photocatalytic performance, the surface work function (φ) was conducted. [57–59] The value of surface work function is
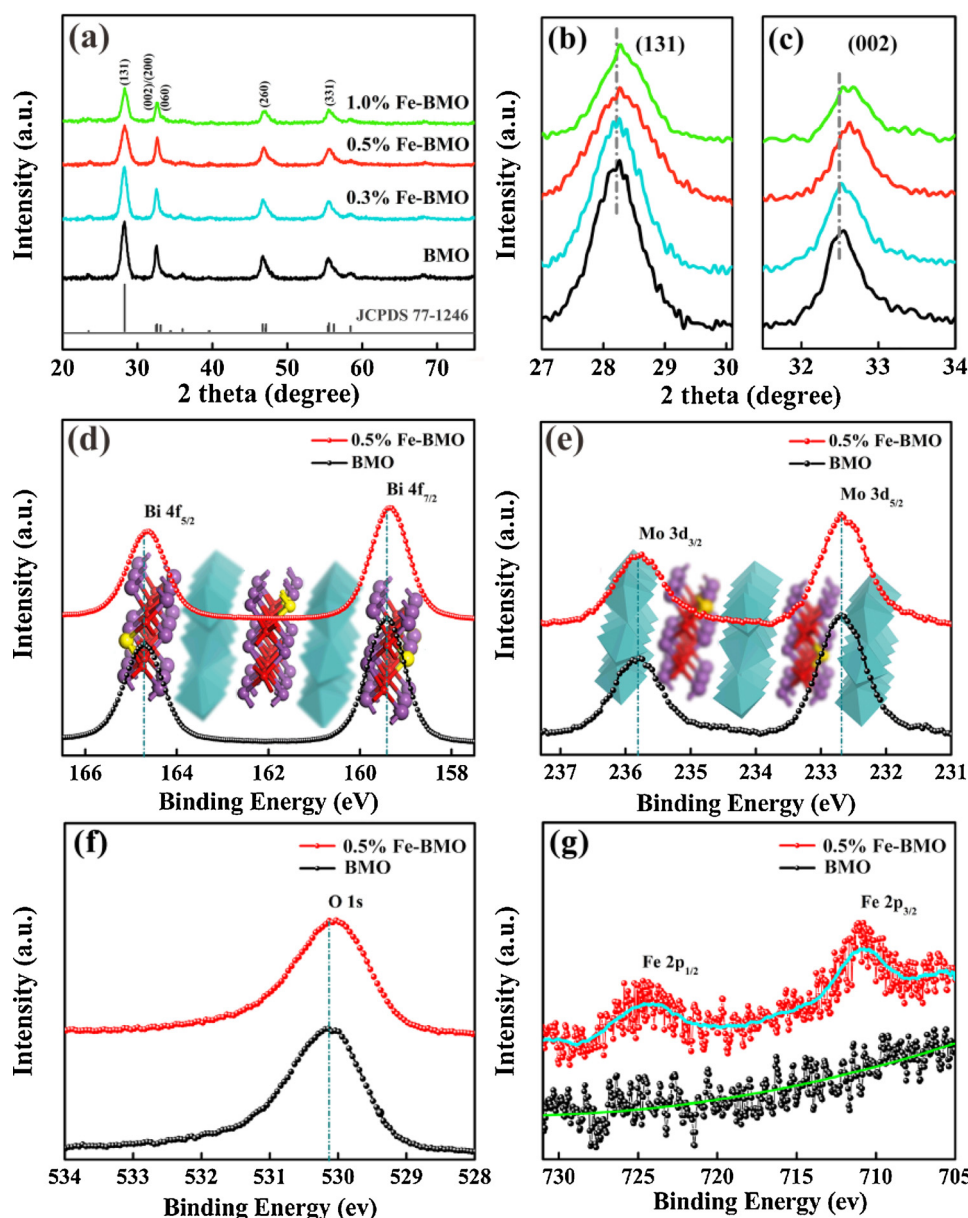
Fig. 2. (a, b) XRD patterns of BMO, 0.3% Fe-BMO, 0.5% Fe-BMO and 1.0% Fe-BMO; (d–g) XPS spectra of BMO and 0.5% Fe-BMO for Bi 4f, Mo 3d, O 1s and Fe 2p.

calculated according to the following formula (1):

$$\varphi_{Au} - \frac{\eta_{Au}}{1000} = \varphi - \frac{\eta}{1000} \quad (1)$$

Where φ_{Au} is the work function of Au ($\varphi_{Au} = 5.1$ eV), $\eta_{Au} = -239.75$ eV. [60] As shown in Fig. 5a–d, the calculated surface work functions (φ) are 5.22, 5.01, 4.91, and 5.16 eV for BMO, 0.3%, 0.5%, and 1.0% Fe^{3+} doping BMO samples, respectively. The first-principles simulations confirm that the surface work function is reduced after Fe^{3+} doping (Fig. 6a and b). In principle, the level of work function is determined by the Fermi level of semiconductor material, which is approximately the same as the flat band potential position for a typical n-type semiconductor. Therefore, the Mott-Schottky measurement was implemented to confirm the flat band potential positions of samples. As shown in Fig. 7a and 7b, the flat band potential (Fermi level) of Bi_2MoO_6 increases after Fe^{3+} doping, which leads to a decrease in the surface work function. Moreover, a lower surface work function with weaker electron binding restriction capacity and more pronounced surface band bending can effectively accelerate the photo-induced charge migration and separation. [45] In addition, the work function

value tends to rise as the doping amount increases. It is speculated that excessive doping will form the trapping center for carriers in the bulk of catalyst, thus the carriers migration to the surface is suppressed. This is well consistent with the photocatalytic activities of the samples.

Apart from decreased surface work function, the charge collection behavior is further determined by photoelectrochemical measurement. The flat band potential of 0.5% Fe-BMO shifts to positive potential under light irradiation, while no obvious change occurs in BMO (Fig. 7a and b). This difference infers that Fe-doping achieves photogenerated charges storage in Bi_2MoO_6. To further confirm the photogenerated charges storage in Fe-doped Bi_2MoO_6, the transient photocurrent test is implemented. The striking jumps and following decays of the photocurrent in the photoanode based on Fe-doped BMO are observed after switching the light on/off Fig. 7c. This result demonstrates that Fe-doped BMO appears to behave on charging and discharging similar to an electronic capacitor consistent with the results confirmed in the literature. [61] Moreover, 0.5% Fe-BMO yields a higher photocurrent density compared to pristine BMO, indicating the Fe-doping can improved the separation efficiency of photogenerated carriers,
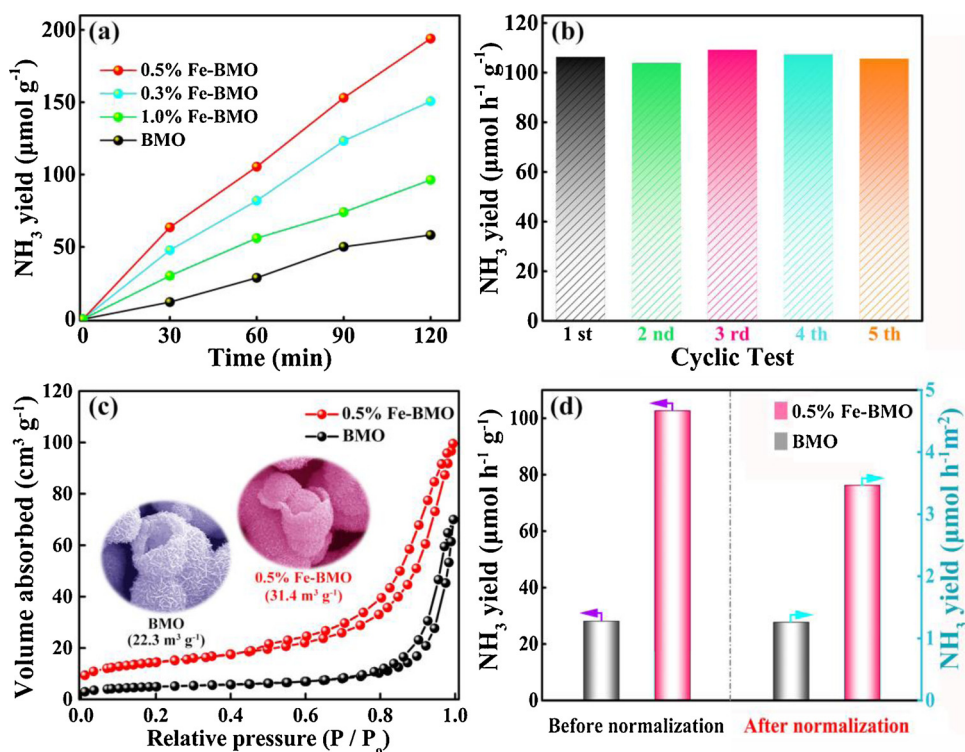
Fig. 3. (a) Photocatalytic nitrogen fixation of BMO, 0.3% Fe-BMO, 0.5% Fe-BMO and 1.0% Fe-BMO under visible-light irradiation; (b) Stability test for the visible-light nitrogen fixation over 0.5% Fe-BMO; (c) Nitrogen adsorption-desorption isotherm and (d) The normalized comparison for photocatalytic nitrogen fixation performance according to the specific surface area over BMO and 0.5% Fe-BMO.

significantly. The Nyquist plots reveal that the arc radius for 0.5% Fe-BMO sample decreases prominently as compared to BMO (Fig. 7d), which demonstrate that the Fe-doping can indeed promote the photo-induced carriers transport. In addition, the EIS of BMO and 0.5% Fe-BMO were also analyzed in dark and under light illumination (Fig. S14). After illumination, the arc radius of 0.5% Fe-BMO decreases more significantly than that of BMO. The possibility reason could attributed to the decreased surface work function of Bi_2MoO_6 after Fe doping, which caused the transport resistance of carriers decreased obviously compared with pure phase BMO under illumination conditions. On the basis of above analysis, the Fe-doping can endow BMO with charge storage ability, which significantly facilitate the photogenerated charge transport.

With the purpose of further probing in-depth the kinetic behavior of carriers, the photoluminescence (PL) measurement was performed. The PL signal of the samples are detected under an excitation light of 365 nm as displayed in Fig. 8a. Compared with the strong emission peaks for BMO, 0.5% Fe-BMO displays rather weak PL peak, indicating that charge storage ability can effectively restrict the electron-hole recombination. From the observation in time-resolved fluorescence decay spectra (Fig. 8b), the decay kinetics of 0.5% Fe-BMO (14.29 ns) is relatively slow than that of BMO (9.21 ns). [62–64] The increased lifetimes of carriers in 0.5% Fe-BMO indicate the improved carriers migration and transport to the photocatalytic reaction sites.

In consequence, a hypothetical photocatalytic nitrogen fixation process with the Fe-doping BMO was proposed as shown in Fig. 9. Under the visible light irradiation, the electrons in the valence band are excited to the conduction band and then generate photo-generated
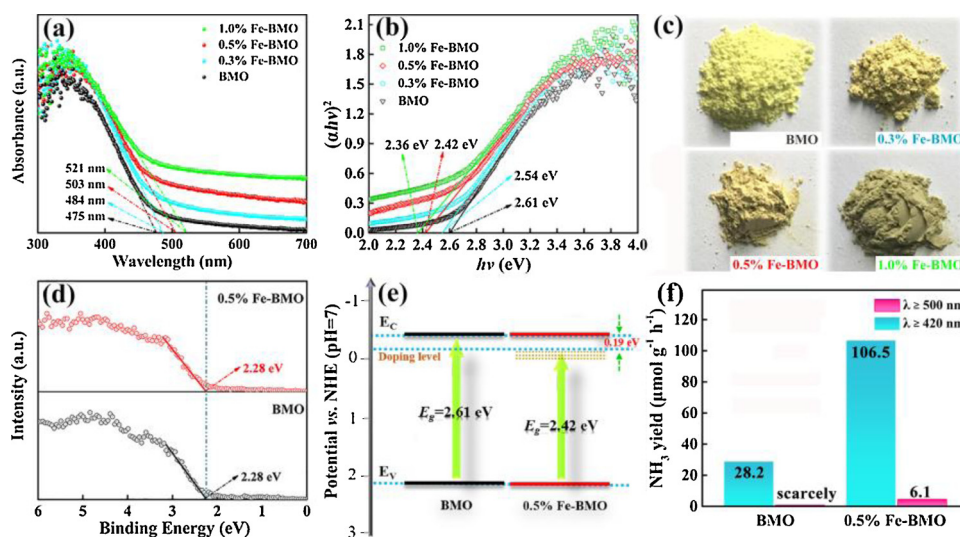

Fig. 4. (a) UV–vis absorption spectrum, (b) Tauc plots, (c) Sample color of BMO, 0.3% Fe-BMO, 0.5% Fe-BMO and 1.0% Fe-BMO; (d) XPS valence band spectra, (e) Electronic band structure and (f) Photocatalytic nitrogen fixation under visible light irradiation (λ > 500 nm) of BMO and 0.5% Fe-BMO.
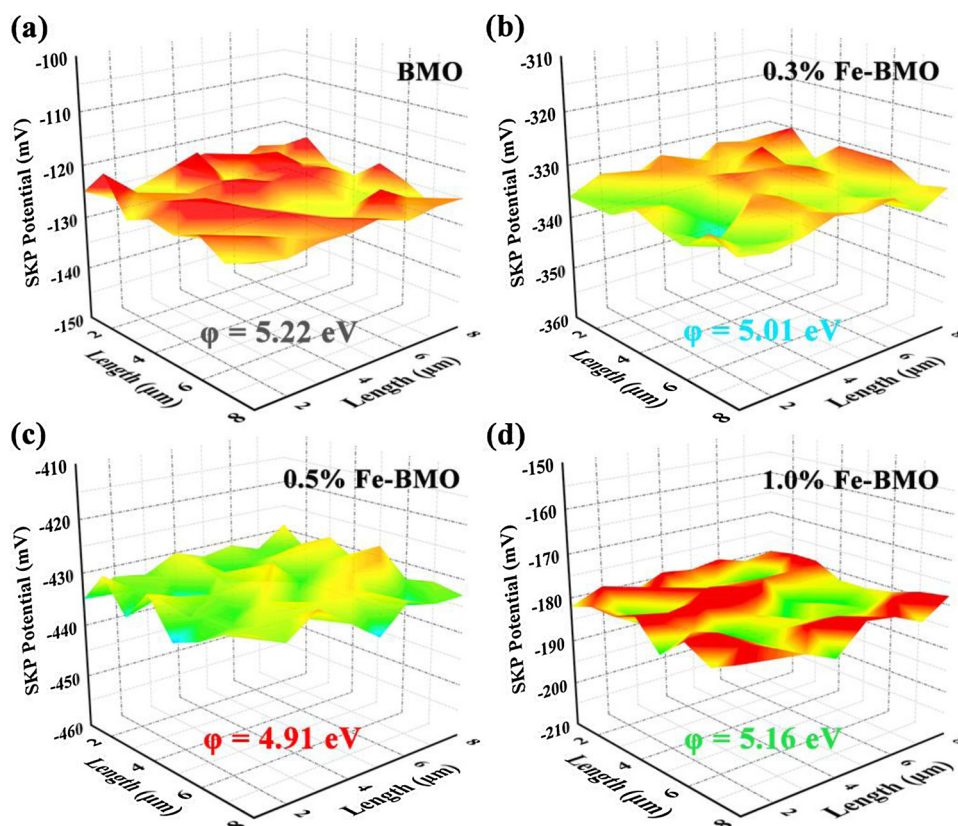
Fig. 5. Relative work function maps of (a) BMO, (b) 0.3% Fe-BMO, (c) 0.5% Fe-BMO and (d) 1.0% Fe-BMO.

carriers. Afterwards, the carriers migrate to the surface for participate in the surface reaction. The holes will directly react with the OH^- adsorbed on the surface to produce O_2 (Fig. S15) and H_2O. For the electrons, a part of electrons will react directly with N_2 to reduce it to NH_3. And another part of the electrons may reduce the doped Fe^{3+} to Fe^{2+} ions, further activating N_2 molecules to produce NH_3. Then Fe^{2+} is oxidized to Fe^{3+} ions by the O_2 generated during the reaction, which accelerates the consumption of holes and promotes the nitrogen fixation reaction. Thus, BMO is possessed with the charge storage ability by reduces the surface work function and acts as an active site on the semiconductor surface, which significantly facilitate the photo-generated charge transport and separation. Furthermore, the sample of Fe^{3+} doped BMO exhibits excellent photocatalytic nitrogen fixation activity.

3.1. Conclusions

In summary, Fe-mediated Bi_2MoO_6 was successfully obtained with outstanding photocatalytic nitrogen fixation performance. Specifically, compared to pristine BMO, 0.5% Fe-BMO presents a 3.7 times promotion of photocatalytic nitrogen fixation activity under visible light irradiation. The Fe-doping act as the surface active sites, leading to effective for N_2 reduction. Moreover, the Fe-doping can reduce the surface function of Bi_2MoO_6, which will integrate with charge storage to synergistically facilitate the photoinduced charge transport. Thus, Fe-mediated Bi_2MoO_6 enables eminent nitrogen fixation performance, which provides opportunities to develop effective photocatalysts for N_2 fixation.
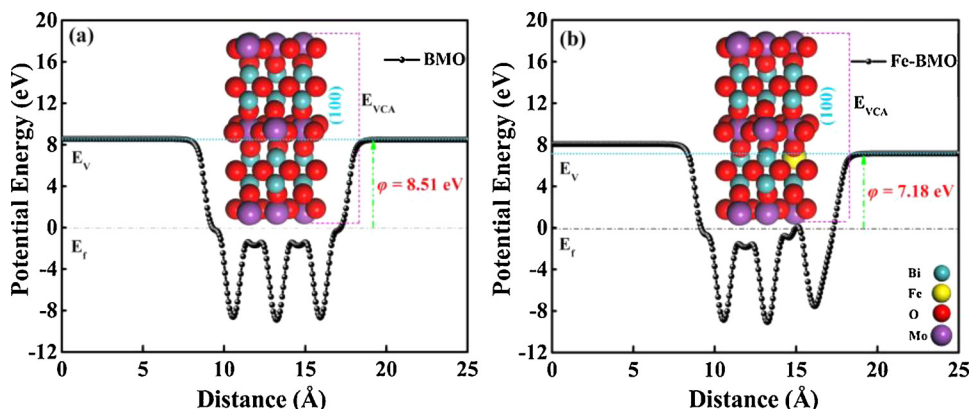

Fig. 6. Potential lineup diagram of (a) BMO and (b) 0.5% Fe-BMO obtained from first-principles simulations where electronic Fermi levels are set to zero.
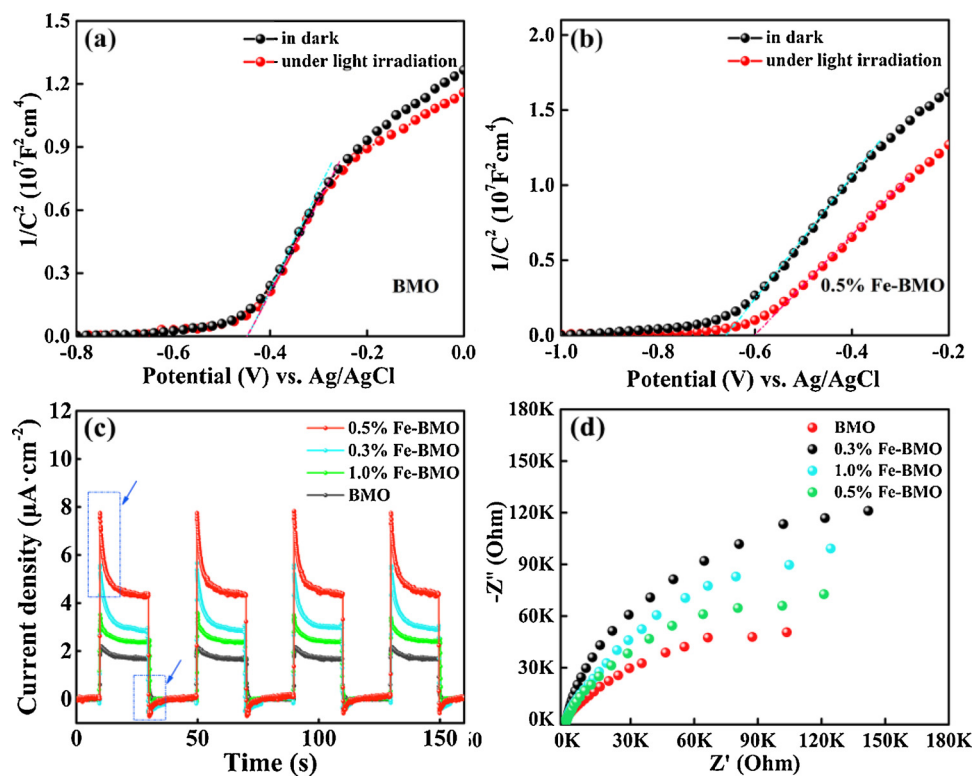
Fig. 7. Mott-Schottky curves in the dark and under light irradiation of (a) BMO and (b) 0.5% Fe-BMO, (c) Photocurrent responses at the applied potential of 0.5 V vs Ag/AgCl and (d) EIS plots of BMO, 0.3% Fe-BMO, 0.5% Fe-BMO and 1.0% Fe-BMO.
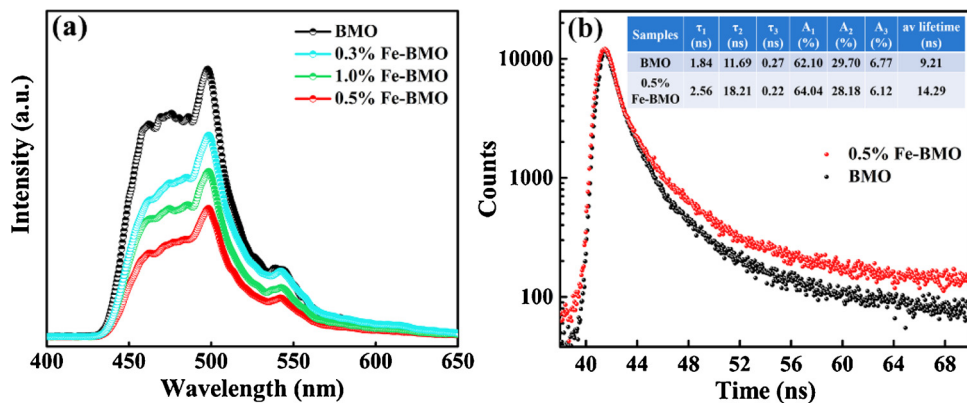

Fig. 8. (a) PL spectra, (b) Time-resolved fluorescence decay spectra of BMO and 0.5% Fe-BMO samples.
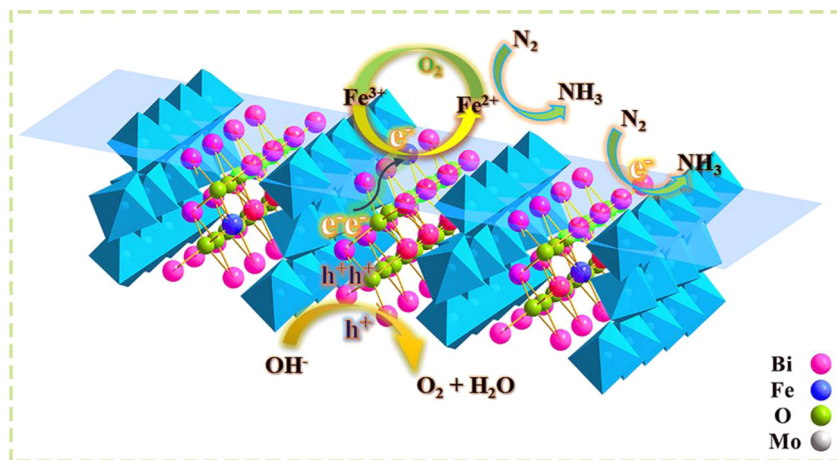

Fig. 9. Schematic diagram of the suppositional photocatalysis process over the 0.5% Fe-BMO sample under visible light irradiation.

4. Associated content

4.1. Supporting information

The image of photocatalytic nitrogen fixation reaction reaction device (Fig. S1); SEM images of (a) BMO, (b) 0.3% Fe-BMO and (c) 1.0% Fe-BMO (Fig. S2); TEM images of (a) BMO, (b) 0.3% Fe-BMO, (b) 0.5% Fe-BMO, (d) 1.0% Fe-BMO (Fig. S3); Structure model illustration of BMO and Fe-BMO samples (Fig. S4); Raman spectra of BMO, 0.3% Fe-BMO, 0.5% Fe-BMO and 1.0% Fe-BMO samples (Fig. S5); (a) The standard curve of photocatalytic nitrogen fixation with Nessler's reagent and (b) The photos of standard solutions (Fig. S6); XRD patterns of 0.5% Fe-BMO before and after cyclic testing (Fig. S7); SEM images of 0.5% Fe-BMO (a) before and (b) after cyclic testing (Fig. S8); (a) The standard curve of photocatalytic nitrogen fixation with indophenol blue method and (b) Photocatalytic nitrogen fixation of BMO and 0.5% Fe-BMO with indophenol blue method and ion chromatography method (Fig. S9); UV–vis measurements of the concentrations of hydrazine hydrate. (a) UV–vis spectra for standard solutions. (b) Calibration curve for hydrazine hydrate concentration vs absorbance (Fig. S10); The amount of NH_3 and N_2H_4 produced on 0.5% Fe-BMO (Fig. S11); (a) The blank experiment and (b) Photocatalytic nitrogen fixation of 0.5% Fe-BMO under different reaction conditions (Fig. S12); (a) Photocatalytic reduction efficiency of Cr(VI) over BMO, 0.3% Fe-BMO, 0.5% Fe-BMO and 1.0% Fe-BMO; (b) Photocatalytic reduction of Cr(VI) with five separate cycles (Fig. S13) The Nyquist plots of BMO and 0.5% Fe-BMO in dark and under light illumination (Fig. S14); Photocatalytic O_2 production rate of BMO and 0.5% Fe-BMO (Fig. S15).

Acknowledgements

Appendix A. Supplementary data

Supplementary material related to this article can be found, in the online version, at doi:https://doi.org/10.1016/j.apcatb.2019.117781.

References

[1] S.Y. Wang, F. Ichihara, H. Pang, H. Chen, J.H. Ye, Nitrogen fixation reaction derived from nanostructured catalytic materials, Adv. Funct. Mater. (2018) 1803309.

[2] X. Chen, N. Li, Z. Kong, W.J. Ong, X. Zhao, Photocatalytic fixation of nitrogen to ammonia: state-of-the-art advancements and future prospects, Mater. Horiz. 5 (2018) 9–27.

[3] Y. Zhao, Y. Zhao, G.I.N. Waterhouse, L. Zheng, X. Cao, Layered-double-hydroxide nanosheets as efficient visible-light-driven photocatalysts for dinitrogen fixation, Adv. Mater. 29 (2017) 1703828.

[4] C.D. Lv, Y.M. Qian, C.S. Yan, Y. Ding, Y.Y.Liu.G. Chen, G.H. Yu, Defect engineering metal-free polymeric carbon nitride electrocatalyst for effective nitrogen fixation under ambient conditions, Angew. Chem. Int. Ed. 57 (2018) 10246–10250.

[5] Z.W. Fang, G.H. Yu, Single atom catalyst towards ammonia synthesis at mild conditions, Sci. China Chem. 61 (2018) 1045–1046.

[6] S. Wang, X. Hai, X. Ding, K. Chang, Y.G. Xiang, J.H. Ye, Light-switchable oxygen vacancies in ultrafine Bi5O7Br nanotubes for boosting solar-driven nitrogen fixation in pure water, Adv. Mater. 29 (2017) 1701774.

[7] C.D. Lv, C.S. Yan, G. Chen, Y. Ding, J. Sun, Y.S. Zhou, G.H. Yu, An amorphous noble-metal-free electrocatalyst that enables nitrogen fixation under ambient conditions, Angew. Chem. Int. Ed. 130 (2018) 6181–6184.

[8] L.Q. Ye, C.Q. Han, Z.Y. Ma, Y.M. Leng, J. Li, X.X. Ji, Z.X. Huang, Ni2P loading on Cd₀.₅Zn₀.₅S solid solution for exceptional photocatalytic nitrogen fixation under visible light, Chem. Eng. J. 307 (2017) 311–318.

[9] C.L. Xiao, L.Q. Ye, T. Chen, L. Wang, X. Shi, X. Zhang, D. Chen, A new approach to enhance photocatalytic nitrogen fixation performance via phosphate-bridge: a case study of SiW₁₂/K-C₃N₄, Appl. Catal. B: Environ. 239 (2018) 260–267.

[10] C. Guo, J. Ran, A. Vasileff, S.Z. Qiao, Rational design of electrocatalysts and photo (electro) catalysts for nitrogen reduction to ammonia (NH₃) under ambient conditions, Energy Environ. Sci. 11 (2018) 45–56.

[11] J.H. Yang, Y.Z. Guo, R.B. Jiang, High-efficiency "Working-in-Tandem" nitrogen photofixation achieved by assembling plasmonic gold nanocrystals on ultrathin titania nanosheets, J. Am. Chem. Soc. 140 (2018) 8497–8508.

[12] J. Wu, Y.Y. Sun, C.H. Gu, T. Wang, Y.J. Xin, C. Chai, C.Y. Cui, D. Na, Pt supported

and carbon coated Bi₂MoO₆ composite for enhanced 2,4-dibromophenol degradation under visible-light irradiation: Insight into band gap structure and photocatalytic mechanism, Appl. Catal. B: Environ. 237 (2018) 622–632.

[13] Q.Q. Meng, Y.S. Zhou, G. Chen, Y.D. Hu, C.D. Lv, L.S. Qiang, W.N. Xing, Integrating both homojunction and heterojunction in QDs self-decorated Bi₂MoO₆/BCN composites to achieve an efficient photocatalyst for Cr(VI) reduction, Chem. Eng. J. 334 (2018) 334–343.

[14] J.H. Guo, L. Shi, J.Y. Zhao, Y. Wang, K.B. Tang, W.Q. Zhang, C.Z. Xie, X.Y. Yuan, Enhanced visible-light photocatalytic activity of Bi₂MoO₆ nanoplates with heterogeneous Bi₂MoO₆-ₓ@Bi₂MoO₆ core-shell structure, Appl. Catal. B: Environ. 224 (2018) 692–704.

[15] J.S. Cai, J.Y. Huang, Y.K. Lai, Correction: 3D Au-decorated Bi₂MoO₆ nanosheet/ TiO₂ nanotube array heterostructure with enhanced UV and visible-light photocatalytic activity, J. Mater. Chem. A Mater. Energy Sustain. 5 (2017) 16422-16422.

[16] R.A. Buker, C. Greaves, Reduction and reoxidation behaviour of γ-Bi₂MoO₆, J. Catal. 108 (1987) 247–249.

[17] J. Xu, M. Fujitsuka, S. Kin, Z.P. Wang, T. Majima, Unprecedented effect of CO₂ calcination atmosphere on photocatalytic H₂ production activity from water using g-C₃N₄ synthesized from triazole polymerization, Appl. Catal. B: Environ. 241 (2019) 141–148.

[18] J. Tian, P. Hao, N. Wei, H.Z. Cui, H. Liu, 3D Bi₂MoO₆ nanosheet/TiO₂ nanobelt heterostructure: enhanced photocatalytic activities and photoelectochemistry performance, ACS Catal. 5 (2015) 4530–4536.

[19] Z.L. Qiu, J. Shu, D.P. Tang, Plasmonic resonance enhanced photoelectrochemical aptasensors based on g-C₃N₄/Bi₂MoO₆, Chem. Commun. (Camb.) 54 (2018) 7199–7202.

[20] J.L. Lv, J.F. Zhang, J. Liu, Z. Li, K. Dai, C.H. Liang, Bi SPR-promoted Z-scheme Bi₂MoO₆/CdS-diethylenetriamine composite with effectively enhanced visible light photocatalytic hydrogen evolution activity and stability, ACS Sustain. Chem. Eng. 6 (2018) 696–706.

[21] L.N. Song, L. Chen, J. He, P. Chen, H.K. Zeng, C.T. Au, S.F. Yin, The first synthesis of Bi self-doped Bi₂MoO₆–Bi₂Mo₃O₁₂ composites and their excellent photocatalytic performance for selective oxidation of aromatic alkanes under visible light irradiation, Chem. Commun. (Camb.) 53 (2017) 6480–6483.

[22] H.P. Li, J.Y. Liu, W.G. Hou, N. Du, R.J. Zhang, X.T. Tao, Synthesis and characterization of g-C₃N₄/Bi₂MoO₆ heterojunctions with enhanced visible light photocatalytic activity, Appl. Catal. B: Environ. 160-161 (2014) 89–97.

[23] J. Di, J.X. Xia, M.X. Ji, H.P. Li, H. Xu, H.M. Li, R. Chen, The synergistic role of carbon quantum Dots for the improved photocatalytic performance of Bi₂MoO₆, Nanoscale 7 (2015) 11433–11443.

[24] Y. Ma, Z.G. Wang, Y.L. Jia, L.N. Wang, M. Yang, Y.X. Qi, Y.P. Bi, Bi₂MoO₆ nanosheet array modified with ultrathin graphitic carbon nitride for high photoelectrochemical performance, Carbon 114 (2017) 591–600.

[25] A.A. Alemi, R. Kashfi, B. Shabani, Preparation and characterization of novel Ln (Gd³⁺, Ho³⁺ and Yb³⁺)-doped Bi₂MoO₆ with aurivillius layered structures and photocatalytic activities under visible light irradiation, J. Mol. Catal. A Chem. 392 (2014) 290–298.

[26] Z. Zhu, X. Tang, T.S. Wang, W.Q. Fan, Y.S. Yan, Insight into the effect of co-doped to the photocatalytic performance and electronic structure of g-C₃N₄ by first principle, Appl. Catal. B: Environ. 241 (2019) 319–328.

[27] G.N. Schrauzer, T.D. Guth, Photocatalytic reactions. 1. Photolysis of water and photoreduction of nitrogen on titanium dioxide, J. Am. Chem. Soc. 99 (1977) 7189–7193.

[28] C.S. Tian, W.L. Sheng, H. Tan, H. Jiang, C.R. Xiong, Fabrication of lattice-doped TiO₂ nanofibers by vapor-phase growth for visible light-driven N₂ conversion to ammonia, ACS Appl. Mater. Interfaces 10 (2018) 37453–37460.

[29] L. Li, Y.C. Wang, S. Vanka, X.Y. Mu, Z.T. Mi, C.J. Li, Nitrogen photofixation over III-nitride nanowires assisted by ruthenium clusters of low atomicity, Angew. Chem. Int. Ed. 30 (2017) 8827–8831.

[30] O. Rusina, A. Eremenko, G. Frank, H.P. Strunk, H. Kisch, Nitrogen photofixation at nanostructured iron titanate films, Angew. Chem. Int. Ed. 40 (2001) 3993–3995.

[31] W.R. Zhao, J. Zhang, X. Zhu, M.J. Tang, M. Tian, Y. Wang, Enhanced nitrogen photofixation on Fe-doped TiO₂ with highly exposed (101) facets in the presence of ethanol as scavenger, Appl. Catal. B: Environ. 144 (2014) 468–477.

[32] J. Soria, J.C. Conesa, V. Augugliaro, Dinitrogen photoreduction to ammonia over titanium dioxide powders doped with ferric ions, J. Phys. Chem. C 95 (1991) 274–282.

[33] Q.D. Zhao, D.J. Wang, L.L. Peng, Y.H. Lin, M. Yang, T.F. Xie, Surface photovoltage study of photogenerated charges in ZnO nanorods array grown on ITO, Chem. Phys. Lett. 434 (2007) 96–100.

[34] N.A. Yakusheva, V.G. Pogadaev, Doping of GaAs with donor impurities Te and Sn during liquid phase epitaxy from mixed gallium bismuth melts, Cryst. Res. Technol. 27 (1992) 21–30.

[35] J.R. Ran, W.W. Guo, H.L. Wang, B.C. Zhu, J.G. Yu, S.Z. Qiao, Metal-free 2D/2D phosphorene/g-C₃N₄ van der Waals heterojunction for highly enhanced visible-light photocatalytic H₂ production, Adv. Mater. 30 (2018) 1800128.

[36] Y.X. Zhao, R. Shi, X.A. Bian, C. Zhou, Y.F. Zhao, S. Zhang, T.R. Zhang, Ammonia detection methods in Photocatalytic and electrocatalytic experiments: how to improve the reliability of NH₃ production rates? Adv. Sci. (2019) 1802109.

[37] J. Liu, M.S. Kelley, W.Q. Wu, A. Banerjee, A.P. douvalis, J.S. Wu, Y.B. Zhang, G.C. Schatz, M.G. Kanatzidis, nitrogenase-mimic iron-containing chalcogels for photochemical reduction of dinitrogen to ammonia, PNAS 113 (2016) 5530–5535.

[38] B.J. Sun, W. Zhou, H.Z. Li, L.P. Ren, P.Z. Qiao, W. Li, H.G. Fu, Synthesis of particulate hierarchical tandem heterojunctions toward optimized photocatalytic hydrogen production, Adv. Mater. 30 (2018) 1804282.

[39] J.L. Long, S.C. Wang, H.J. Chang, B.Z. Zhao, B.T. Liu, Y.G. Zhou, W. Wei,

X.X. Wang, L. Huang, W. Huang, Bi_2MoO_6 nanobelts for crystal facet-enhanced photocatalysis, Small 10 (2014) 2791–2795 2741.

[40] J.P. Zou, S.L. Luo, L.Z. Zhang, J. Ma, S.L. Lei, L.S. Zhang, X.B. Luo, Y. Luo, G.S. Zeng, C.T. Au, One-pot solvothermal syntheses of ternary heterostructured TiO_2–Bi_2MoO_6/$Bi_{3.64}Mo_{0.36}O_{6.55}$ controllable in terms of composition, morphology and structure: materials of high visible-light driven photocatalytic activity, Appl. Catal. B: Environ. 140-141 (2013) 608–618.

[41] J. Zhang, C.G. Niu, J. Ke, L.F. Zhou, G.G. Zeng, Ag/AgCl/Bi_2MoO_6 composite na-nosheets: a plasmonic Z-scheme visible light photocatalyst, Catal. Commun. 59 (2015) 30–34.

[42] Y. Ma, Y.L. Jia, Z.B. Jiao, M. Yang, Y.X. Qi, Y.P. Bi, Hierarchical Bi_2MoO_6 na-nosheet-built frameworks with excellent photocatalytic properties, Chem. Commun. (Camb.) 51 (2015) 6655–6658.

[43] N.C. Birben, C.S. Uyguner-Demirel, S. Sen Kavurmaci, Y.Y. Gurkan, N. Turkten, Z. Cinar, M. Bekbolet, Application of Fe-doped TiO_2 specimens for the solar pho-tocatalytic degradation of humic acid, Catal. Today 281 (2017) 78–84.

[44] C.Y. Xu, Y.W. Zhang, J.C. Chen, J.Y. Lin, X.H. Zhang, Z.H. Wang, J.H. Zhou, Enhanced mechanism of the photo-thermochemical cycle based on effective Fe-doping TiO_2 films and DFT calculations, Appl. Catal. B: Environ. 204 (2017) 324–334.

[45] Z. Dai, F. Qin, H. Zhao, J. Ding, Y. Liu, R. Chen, Crystal defect engineering of aurivillius Bi_2MoO_6 by Ce doping for increased reactive species production in photocatalysis, ACS Catal. 6 (2016) 3180–3192.

[46] Z. Dai, F. Qin, H.P. Zhao, F. Tian, Y.L. Liu, R. Chen, Time-dependent evolution of the $Bi_{3.64}Mo_{0.36}O_{6.55}$/$Bi_2MoO_6$ heterostructure for enhanced photocatalytic activity via the interfacial hole migration, Nanoscale 7 (2015) 11991–11999.

[47] Y.G. Zhou, S. Zhang, Y. Ding, L.Y. Zhang, C.K. Zhang, X.H. Zhang, Y. Zhao, G.H. Yu, Efficient solar energy harvesting and storage through a robust photocatalyst driving reversible redox reactions, Adv. Mater. 30 (2018) 1802294.

[48] Y.J. Chen, G.H. Tian, Y.H. Shi, Y.T. Xiao, H.G. Fu, Hierarchical MoS_2/Bi_2MoO_6 composites with synergistic effect for enhanced visible photocatalytic activity, Appl. Catal. B: Environ. 164 (2015) 40–47.

[49] T.J. Ma, J. Wu, Y.D. Mi, Q.H. Chen, D. Ma, C. Chai, Novel Z-scheme g-C3N4/C@ Bi2MoO6 composite with enhanced visible-light photocatalytic activity for β-naphthol degradation, Sep. Purif. Technol. 183 (2017) 54–65.

[50] Y.G. Zhou, L.Y. Zhang, L.H. Lin, B.R. Wygant, Y. Liu, Y. Zhu, Y.B. Zheng, C.B. Mullins, Y. Zhao, X.H. Zhang, G.H. Yu, Highly efficient photoelectrochemical water splitting from hierarchical WO_3/$BiVO_4$ nanoporous sphere arrays, Nanosci. Nanotechnol. Lett. 17 (2017) 8012–8017.

[51] K.Q. Jing, W. Ma, Y.H. Ren, J.H. Xiong, B.B. Guo, Y.J. Song, S.J. Jiang, L. Wu, Hierarchical Bi_2MoO_6 spheres in situ assembled by monolayer nanosheets toward photocatalytic selective oxidation of benzyl alcohol, Appl. Catal. B: Environ. 243

(2019) 10–18.

[52] H.D. Li, W.J. Li, F.Z. Wang, X.T. Liu, C.J. Ren, Fabrication of two lanthanides co-doped Bi_2MoO_6 photocatalyst: selection, design and mechanism of Ln1/Ln2 redox couple for enhancing photocatalytic activity, Appl. Catal. B: Environ. 217 (2017) 378–387.

[53] J. Ke, X.G. Duan, S. Luo, H.Y. Zhang, H.Q. Sun, J. Liu, M. Tade, S.B. Wang, UV-assisted construction of 3D hierarchical rGO/Bi_2MoO_6 composites for enhanced photocatalytic water oxidation, Chem. Eng. J. 313 (2017) 1447–1453.

[54] M. Wang, M.Y. You, P.Y. Guo, H.Y. Tang, C.M. Lv, Y. Zhang, T. Zhu, J. Han, Hydrothermal synthesis of Sm-doped Bi_2MoO_6 and its high photocatalytic perfor-mance for the degradation of rhodamine B, J. Alloys. Compd. 728 (2017) 739–746.

[55] H.P. Li, Q.H. Deng, J.Y. Liu, W.G. Hou, N. Du, R.J. Zhang, X.T. Tao, Synthesis, characterization and enhanced visible light photocatalytic activity of Bi_2MoO_6/Zn–Al layered double hydroxide hierarchical heterostructures, Catal. Sci. Technol. 4 (2014) 1028.

[56] B.J. Jin, Z.B. Jiao, Y.P. Bi, Efficient charge separation between Bi_2MoO_6 nanosheets and ZnO nanowires for enhanced photoelectrochemical properties, J. Mater. Chem. A Mater. Energy Sustain. 3 (2015) 19702–19705.

[57] D. Singh, S.K. Gupta, Y. Sonvane, A. Kumar, R. Ahuja, 2D-HfS_2 as an efficient photocatalyst for water splitting, Catal. Sci. Technol. 6 (2016) 6605–6614.

[58] A.P. Wu, C.G. Tian, H.J. Yan, Y.Q. Jiao, Q. Yan, G.Y. Yang, H.G. Fu, Hierarchical MoS_2@mop core-shell heterojunction electrocatalysts for efficient hydrogen evo-lution reaction over a broad pH range, Nanoscale 8 (2016) 11052–11059.

[59] N. Zhang, A. Jalil, D.X. Wu, S.M. Chen, Y.F. Liu, C. Gao, W. Ye, Z.M. Qi, Refining defect states in $W_{18}O_{49}$ by Mo doping: a strategy for tuning N_2 activation towards solar-driven nitrogen fixation, J. Am. Chem. Soc. 140 (2018) 9434–9443.

[60] L.L. Bi, X.P. Gao, L.J. Zhang, D.J. Wang, X.X. Zou, T.F. Xie, Enhanced photocatalytic hydrogen evolution of NiCoP/g-C_3N_4 with improved separation efficiency and charge transfer efficiency, Chem. Sus. Chem. 11 (2018) 276–284.

[61] Y.Q. Yang, G. Liu, J.T.S. Irvine, H.M. Cheng, Enhanced photocatalytic H_2 produc-tion in core–shell engineered rutile TiO_2, Adv. Mater. 28 (2016) 5850–5856.

[62] X.J. Kong, Z. Lin, Z.M. Zhang, T. Zhang, W. Lin, Hierarchical integration of pho-tosensitizing Metal-Organic Frameworks and nickel-containing polyoxometalates for efficient visible-light-driven hydrogen evolution, Angew. Chemie Int. Ed. English 55 (2016) 6411–6416.

[63] H.Q. Xu, J. Hu, D. Wang, Z. Li, Q. Zhang, Y. Luo, S.H. Yu, H.L. Jiang, Visible-light photoreduction of CO_2 in a Metal–organic Framework: boosting electron–hole se-paration via electron trap states, J. Am. Chem. Soc. 137 (2015) 13440–13443.

[64] W.T. Bi, L. Zhang, Z.T. Sun, X.G. Li, T. Jin, X.J. Wu, Q. Zhang, Y. Luo, C.Z. Wu, Y. Xie, Insight into electrocatalysts as co-catalysts in efficient photocatalytic hy-drogen evolution, ACS Catal. 6 (2016) 4253–4257.